Applied Materials Today 26 (2022) 101279

Contents lists available at ScienceDirect

Applied Materials Today

journal homepage: www.elsevier.com/locate/apmt

Octacalcium phosphate crystals including a higher density dislocation improve its materials osteogenecity

Ryo Hamai[a,1], Susumu Sakai[a,1], Yukari Shiwaku[a,b], Takahisa Anada[a,c], Kaori Tsuchiya[a], Takuya Ishimoto[d], Takayoshi Nakano[d], Osamu Suzuki[a,*]

[a] Division of Craniofacial Function Engineering, Tohoku University Graduate School of Dentistry, 4-1 Seiryo-machi, Aoba-ku, Sendai 980-8575, Japan
[b] Liaison Center for Innovative Dentistry, Tohoku University Graduate School of Dentistry, Japan
[c] Institute for Materials Chemistry and Engineering, Kyushu University, Japan
[d] Division of Materials and Manufacturing Science, Graduate School of Engineering, Osaka University, Japan

ARTICLE INFO

Article history:
Received 7 July 2021
Revised 29 October 2021
Accepted 15 November 2021

Keywords:
Octacalcium phosphate
Dislocation
Lattice strain
Dissolution
Osteogenecity

ABSTRACT

Herein, we show that the enhanced osteogenecity of octacalcium phosphate (OCP) biomaterial, recently identified as an important element in hybrid organic–inorganic nanocomposites involved in the initial hydroxyapatite crystal expansion in mammal bones, results from an enhanced chemical property, stemming from the presence of lattice strain and dislocations. Two types of OCPs were synthesized by wet-chemical processing in the presence (c-OCP) and absence (w-OCP) of gelatin, respectively, and subjected to structural, chemical, and biological analyses. High-resolution transmission electron microscopy (HRTEM) and fast Fourier transform (FFT) analyses revealed that c-OCP crystals contained approximately six times higher edge dislocations with Burgers vectors perpendicular to *a*-axis than that in the case of w-OCP. The dissolution of c-OCP crystal in tris-HCl buffer occurred toward the long axis of the crystal, most likely, toward the lattice strain along the *c*-axis direction, while w-OCP crystal dissolved toward the *a*-axis direction. The study suggested that the increment of internal energy by the higher dislocation density contributed promoting c-OCP dissolution and hydrolysis through decreasing the activation energy. c-OCP crystal displayed enhanced *in vitro* mesenchymal stem 2D cell and 3D spheroid differentiation, *in vivo* bone formation, and apatite crystallographic orientation in critical-sized rat calvarial defect model as compared to w-OCP crystal, at the same time, converting to apatite structure earlier than w-OCP. The present study demonstrates that dislocation-related dissolution along with enhanced conversion of OCP is a determinant in bone induction, which may be relevant to normal bone development utilizing OCP biomaterials.

1. Introduction

Structural defects in most materials control their fundamental properties, in general, deteriorating the physical and chemical performances. For example, hydrogen can be trapped in lattice defects around dislocations in the embrittlement of Ni–Ti superelastic alloys induced by dynamic martensitic transformation [1]. In biological tissues, tooth enamel dental caries caused by an acid attack was shown to commence with structural defects, such as edge dislocation, in enamel apatite crystals [2]. On the contrary, a recent report suggests that the practical use of the dislocation allows the substrate surface to have a positive effect on the cellular activity in the material [3]. It would be essential to know whether the structural modification in materials used in implant synthetic biomaterials displays certain positive effects in maintaining homeostasis and self-organizing mammalian biological tissues around the materials, which could provide some clues for designing highly bioactive synthetic biomaterials. The present article provides evidence that introducing dislocation and strain into an inorganic octacalcium phosphate (OCP) material can induce a bioactive capacity associated with the chemical properties under physiological conditions. OCP has recently been approved as a substitute material for human oral bone defects [4] due to its osteoconductive and biocompatible properties [5,6]. Previous studies elucidated that the higher osteoconductivity of OCP than hydroxyapatite (HA) is acquired associated with activating osteoblast, osteoclast and osteocyte func-

* Corresponding author.
E-mail address: suzuki-o@tohoku.ac.jp (O. Suzuki).
[1] These authors contributed equally to this work.

https://doi.org/10.1016/j.apmt.2021.101279

tions brought about by their structural difference [5,7–9]: (1) OCP tends to hydrolyze toward Ca-deficient HA (CDHA) under physiological condition, which is accompanied by calcium ion (Ca^{2+}) incorporation and inorganic phosphate (Pi) ion release [10]; (2) the reduction of Ca^{2+} concentration around OCP induces osteoblastic cell differentiation of stromal cells through activating p38 mitogen-activated protein kinase (MAPK) signaling [11]; (3) the reduction of Ca^{2+} concentration around OCP induced osteoclast formation from bone marrow macrophages by inducing co-present osteoblast receptor activator of NF-κB ligand (RANKL) expression through possible calcium sensing receptor in osteoblasts [12]; (4) the increase of Pi ion concentration around OCP enhances osteocyte differentiation from osteoblastic cells, a clonal cell line IDG-SW3, via Pi ion transport in the cells [13]. Therefore, controlling the dissolution and the hydrolysis of OCP through the structural and chemical modifications is essential in increasing the osteoconductivity of the OCP materials. OCP has been demonstrated to be a precursor for formation of HA from supersaturated solutions with respect to HA over three decades ago [14]. OCP has been advocated as a precursor of biological bone apatite crystals, ever since its structure was explicated [15].

The chemical composition of OCP is expressed as $Ca_8H_2(PO_4)_6{\cdot}5H_2O$. The lattice parameters of the unit cells are a = 19.692 Å, b = 9.523 Å, c = 6.835 Å, α = 90.15°, β = 92.54°, γ = 108.65°, and Z = 2 [16,17]. The structure of OCP consists of apatite layers stacked with a hydrated layer in an alternating manner; therefore, it closely resembles the structure of HA ($Ca_{10}(PO_4)_6(OH)_2$), known as the prototype for bone apatite crystals [15,18,19]. Recently, the OCP phase was revealed to be enclosed within a nanocomposite together with a non-collagenous bone-related protein called osteocalcin, under a high-resolution transmission electron microscope (HRTEM), where the bone HA crystal development begins from the OCP-protein nanocomposite to form mammal bone tissues [20]. Interestingly, a synthetic, well-grown OCP implanted in bone tissues can be converted to a bone-like apatitic CDHA crystal progressively with time, in a manner similar to the bone crystal maturation process. This significantly enhanced new bone formation around its surface more than what the synthetic HA implant did [5,6]. However, whether the structural defects are inherent in synthetic OCP and, if so, whether they affect the biological performance of the material, and whether artificially introduced structural defects may strengthen or weaken its biomaterial functioning, have not been elucidated so far.

It is widely accepted that bone apatite crystals consist of non-stoichiometric compositions having structural defects at calcium ion sites and phosphate ion lattice positions, which are replaced with cationic and anionic ions, respectively, such as hydrogen and carbonate ions, and are therefore defined as CDHA [15,18]. Such a crystal defect can also be included in the OCP structure [21] and has been reported to exhibit non-stoichiometric composition [17]. Ca-deficient OCP, having an ion complex composition, $[Ca_6(HPO_4)_4(PO_4)_2]^{2-}$, has been postulated to be present as a series of cluster formations together with the amorphous calcium phosphate ion complex $[Ca_2(HPO_4)_3]^{2-}$, which is finally crystallized to HA. Its presence successfully explains the apatite crystallization in bone mineralization processes [22]. From the perspective of biomaterials, partially hydrolyzed OCP with a slightly higher calcium to phosphate (Ca/P) molar ratio (1.37) as compared to the stoichiometric ratio (1.33), has displayed significantly higher bioactivity than that of the original OCP, regarding bone formation capacity [5,8]. These studies suggest certain clues for developing more bioactive materials, once it is elucidated as to how the structural deficiency contributes to the increased bioactivity [5,8,17,21]. In the formation of human bone apatite crystals, HRTEM and fast Fourier transform (FFT) analysis identified the inclusion of the remarkable lattice distortions in the initial OCP formation, involving a bone-related protein osteocalcin accumulation before subsequent HA deposition [20], thus, suggesting a functional role of OCP with crystal dislocation in accelerating bone formation.

OCP can be synthesized through the hydrolysis of calcium phosphate seed crystals [23–25] and direct precipitation from supersaturated calcium and phosphate solutions [6,26,27]. There have been reports that the presence of certain molecules other than the constituent elements of calcium and phosphate, such as poly-L-aspartate, affect the morphology of plate-like OCP particles, which was partly explained by the interaction between these molecules and the OCP surfaces in specific crystal planes [28]. In the tooth enamel biomineralization model, such an interaction between the enamel proteins—amelogenin and OCP has been suggested to interpret the enamel crystal elongation toward the long axis of large tooth apatite crystals [29]. We successfully prepared OCP co-precipitated with gelatin molecules which exhibited unique properties of reduced serum protein adsorption [30] and enhanced biodegradation as compared to OCP prepared in the absence of gelatin molecules [31,32].

In this study, we demonstrated that two OCPs with the same crystal structures as defined by X-ray crystallography and wet-synthesized in the presence and absence of gelatin molecules exhibited distinct osteogenic biological performances, both *in vivo* and *in vitro*. These differences may originate from the chemical properties associated with the presence of lattice strain and dislocation, which could possibly have been introduced during the preparation step, in the presence of gelatin molecules.

2. Materials and methods

For experimental details see Supplementary Information Appendix. All procedure of animal experiments in this study were reviewed and approved by the Animal Research Committee of Tohoku University (approval number: 2013DnA-023–1, 2019DnA-014). The protocol conformed to all principles of laboratory animal care and national laws.

Crystals of c-OCP and w-OCP were synthesized according to the synthesis method described in literature [6,33]. The c-OCP crystal was precipitated in the presence of 0.5 wt.% type A gelatin with average molecular weight 50,000 to 100,000. Crystals of c-OCP and w-OCP were observed using a HRTEM. FFT of c-OCP and w-OCP HRTEM images was also performed. The filtered HRTEM images were obtained by inverse FFT process with filtering the spots corresponding to objective lattice refraction in the FFT images at a suitable sized.

Granules of w-OCP and c-OCP (10 mg) packed into filter chambers [34] were implanted into the abdominal subcutaneous pouches of the 12-week-old male Wistar rats. The filter chambers were collected at 2 weeks post-implantation. c-OCP and w-OCP granules (50 mg) were also incubated in 50 mL of 150 mM tris(hydroxymethyl)aminomethane (tris)-HCl buffer at 37 °C for 0–3600 s or 0–15 days. The granules of w-OCP and c-OCP were soaked in simulated body fluid (SBF) [35] at 37 °C for 7 and 15 days. These granules were incubated in tris-HCl buffer containing 0.5 mM Ca^{2+} and 0.5 mM Pi ion at 1 mg·mL^{-1} for 24 h at 37 °C or at 5, 8, and 10 mg·mL^{-1} for 30 s at different temperature. The Ca^{2+} and Pi concentrations, and pH in the collected supernatants were measured to assess the kinetics of dissolution and hydrolysis of OCP. The crystals before (original) and after incubation *in vivo* and *in vitro* (in 150 mM tris-HCl buffer) were observed using transmission electron microscope (TEM) and characterized by selected area electron diffraction (SAED). The OCPs before and after incubation *in vitro* were also analyzed using a powder X-ray diffraction (XRD), Raman spectrometry, and X-ray photoelectron spectrometry (XPS).

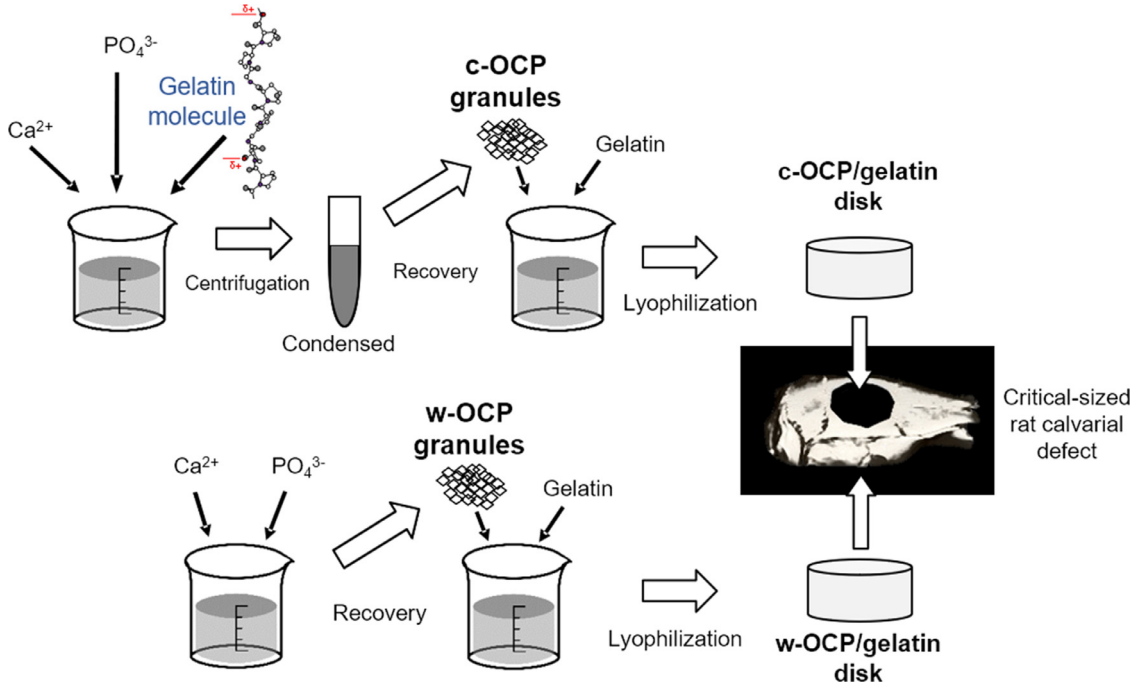

Fig. 1. Schematic illustration of preparation of OCP/Gel composites and the implantation procedure into critical-sized rat calvarial defect (9 mm diameter).

Bone regeneration abilities of the w-OCP/Gel and c-OCP/Gel disks were examined *in vivo*. Wistar rats (12-weeks-old, male) were used for the animal experiments. The procedure of the disks prepared according to previous literature [33,36]. Briefly, the w-OCP or c-OCP granules were mixed with the gelatin solution at 29 and 46 wt.% to the total weight of granules and gelatin (Gel). The mixture was frozen and then lyophilized. The prepared w-OCP/Gel ($n = 5$) and c-OCP/Gel ($n = 5$) disks were implanted into the rat calvarial defects (9 mm diameter). Defects without the treatment were also created ($n = 5$) as a negative control. The schematic illustration of these procedure is shown in Fig. 1. New bone formation induced by implantation of the w-OCP/Gel and c-OCP/Gel disks was evaluated by histomorphometric analysis. Sections prepared from the collected calvarial tissues at 8 weeks post-implantation were stained with hematoxylin and eosin. Photographs of the sections were taken using a slide scanner and then n-Bone% was calculated as the area of newly formed bone per created defect area × 100. Furthermore, apatite orientation of newly formed bone was analyzed by using a microbeam X-ray diffractometer with a transmission optical system.

In cell culture experiments, mouse bone marrow-derived mesenchymal stem cell (MSC) D1 cells (5.0×10^3 cells / well) were seeded with granules of c-OCP ($n = 3$), w-OCP ($n = 3$), and w-OCP in the presence of 5 or 10 wt.% lyophilized gelatin ($n = 3$) in osteogenic differentiation medium on 48 well plate (2D cell culture). D1 cells (1.0×10^6 cells), mixed with c-OCP ($n = 6$) and w-OCP ($n = 6$) granules, were also seeded in the medium on three-dimensional cell culture chips. The 3D cell culture chips were prepared following to previous reports [37,38]. D1 cells in the absence of OCP were also seeded as control groups in 2D (5.0×10^3 cells, $n = 3$) and 3D culture (1.0×10^6 cells, $n = 6$). The supernatants of the culture medium were collected, and the medium was changed every 2 days. The cultured cells were collected at 7, 14, and 21 days to measure DNA concentration and alkaline phosphatase (ALP) activity. Value of ALP activity was normalized to DNA concentration of cells. The value of pH, Ca^{2+} and Pi ion concentrations in the collected medium were also determined to calculate the degree of supersaturation (*DS*) with respect to calcium phosphates in the culture. The c-OCP and w-OCP before and after incubation with spheroids were analyzed using Fourier transform infrared spectrometry (FT-IR) and Raman spectrometry.

Results in the present study are expressed as mean ± standard deviation (SD). For bone histomorphometry, analysis of apatite *c*-axis orientation, and the cell culture experiments, one-way analysis of variance (ANOVA) was used to compare the means among the groups. If the ANOVA was significant, then the Tukey–Kramer multiple comparison analysis was performed. The p values < 0.05 were considered to be statistically significant.

3. Results

3.1. Structural characterization of w-OCP and c-OCP

The c-OCP particles grew into a plate-like shape similar to the w-OCP crystals (Fig. 2A, D). The HRTEM images revealed a clear lattice structure of the plate-like w-OCP crystal (Fig. 2B) as compared to the c-OCP crystals, when put on the cooling stage (Fig. 2E). FFT images of w-OCP (Fig. 2C) and c-OCP (Fig. 2F) were obtained from the HRTEM images of these crystals (Fig. 2B, E). In the images of FFT patterns obtained from the magnified HRTEM, spots appeared at 9.16 Å in the patterns for w-OCP (Fig. 2C) and c-OCP (Fig. 2F) crystals, respectively, which correspond to (010) plane of OCP (9.02 Å). The detected spots at 3.39 Å and 3.30 Å were attributed to (002) plane of OCP (3.41 Å) for the w-OCP and c-OCP crystals, respectively. The angles formed by these two spots and 000 (the spot of center) were 90.8 and 91.0° for w-OCP and c-OCP crystals, respectively, which is in agreement with the angle formed between (010) and (002) planes. The results of FFT indicated that both w-OCP and c-OCP were single crystals of OCP, exposed the *a*-plane on the top surface of the plate particle and oriented toward the *c*-axis.

The lattice fringes with spacings of 3.44 Å (Fig. 2G, H) and 3.34 Å (Fig. 2I, J) were observed in the higher magnified HRTEM images of w-OCP and c-OCP crystals, respectively, which indicate (002) planes in OCP lattice. The fringes with the spacings of 3.07 Å (Fig. 2G, H) and 3.00 Å (Fig. 2I, J) were also observed in the im-

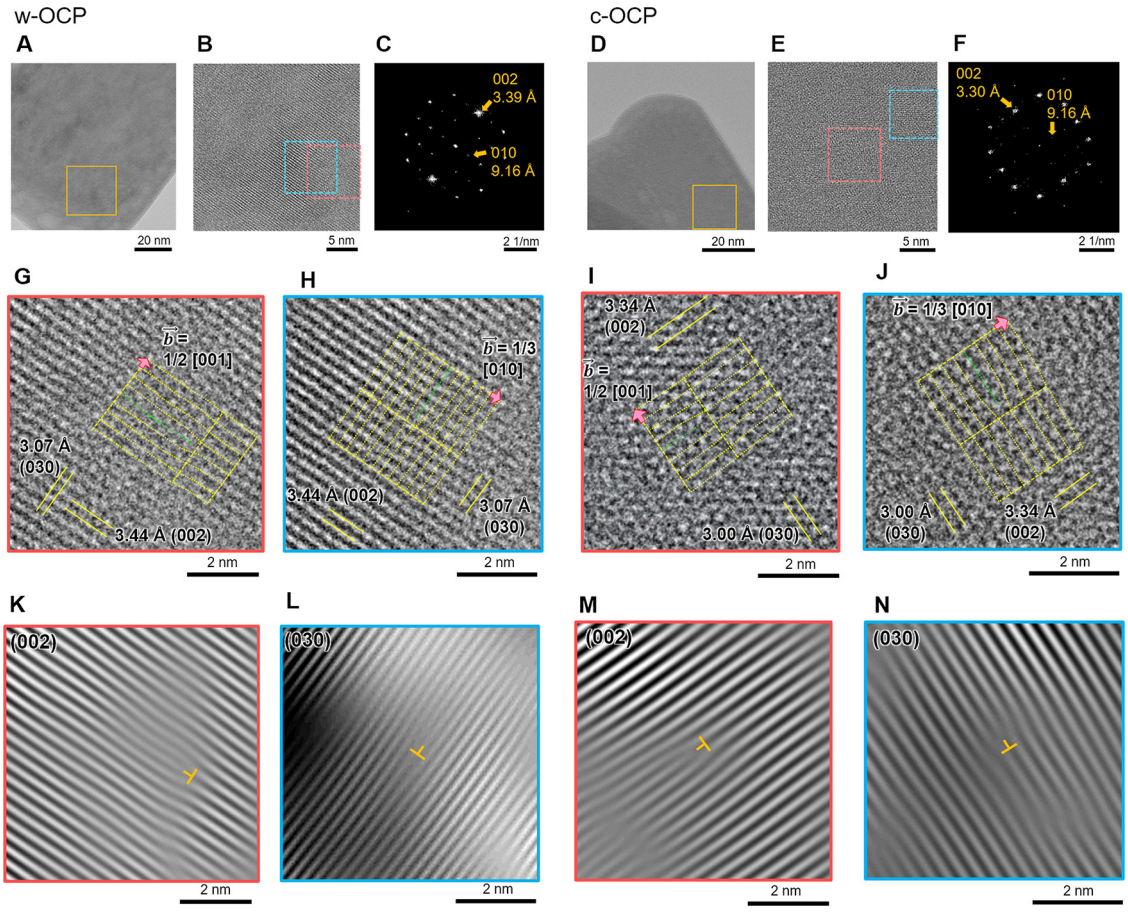

Fig. 2. Structural characterization of synthesized w-OCP and c-OCP crystals. HRTEM images and FFT patterns of synthesized w-OCP (A – C) and c-OCP (D – F) crystals. Yellow open squares in the overview images of w-OCP (A) and c-OCP (D) crystals indicate the regions of lower magnified images of w-OCP (B) and c-OCP (E) crystals, respectively. In the FFT patterns of w-OCP (C) and c-OCP (F) obtained from the lower magnified HRTEM images (B, E), detection of spots attributed to (010) and (002) indicates the reflections along the [100] zone axis of OCP. Higher magnified HRTEM images of w-OCP (G, H) and c-OCP (I,J) in red (G, I) or blue (H, J) squares corresponding to the regions of open red or blue square with broken line in the lower magnified images of them. Green broken lines in the higher magnified images indicate the extra half planes inserted in (002) and (030) of OCP, meaning that the presence of edge dislocations with Burgers vector $\vec{b}$ = 1/2 [001] (G, I) and $\vec{b}$ = 1/3 [010] (H, J), respectively, in both crystals. Yellow broken lines guide the (002) and (030) planes around the edge dislocations. Red arrows indicate Burgers vector of edge dislocation. Filtered HRTEM (inverse FFT) images of w-OCP (K, L) and c-OCP (M, N) obtained by the inverse FFT selecting the reflection corresponding to (002) (K, M) or (030) (L, N) in FFT patterns of w-OCP (C) and c-OCP (F). Regions of filtered images for each crystal in red and bule squares correspond to the higher magnified HRTEM images boxed by red and blue line, respectively. The symbols of ⊥ indicate the positions of edge dislocations in (002) (K, M) or (030) plane (L, N) in the filtered images, which corresponded to the sites of dislocations with $\vec{b}$ = 1/2 [001] (G, I) or $\vec{b}$ = 1/3 [010] (H, J) in the higher magnified HRTEM images, respectively.

ages of w-OCP and c-OCP, respectively, which were attributed to (030) plane of respective OCP. Extra half planes in (002) of OCP were detected in the higher magnified HRTEM images of w-OCP (Fig. 2G) and c-OCP (Fig. 2I), indicating that these crystals included the edge dislocations (line defects) having the Burgers vector of $\vec{b}$ = 1/2 [001]. The extra half planes in (030) of OCP were also observed in the images, which suggests that the edge dislocations with $\vec{b}$ = 1/3 [010] were also contained in these crystals (Fig. 2H, J). Burgers vectors of these edge dislocations oriented in a direction perpendicular to the dislocation line along the *a*-axis of the OCP lattice.

Previous studies applied filtering the images to analyze the details of the structures, such as crystallinity [39] and lattice defects [40]. Simon *et al.* recently visualized the disturbance of the HA lattice formed around osteocalcin by filtering the HRTEM (inverse FFT) image [20]. Filtered HRTEM images of (002) and (030) (Fig. 2K–N) were obtained by the inverse FFT process selecting the spots corresponding to the objective lattice in the FFT patterns (Fig. 2C, F) of these crystals. The positions of extra half planes in (002) planes of w-OCP (Fig. 2K) and c-OCP (Fig. 2M) were displayed in the filtered images, which coincided with the sites of edge dislocations having $\vec{b}$ = 1/2 [001] detected in the HRTEM images of w-OCP (Fig. 2G) and c-OCP (Fig. 2I), respectively. The positions of extra half planes in (030) shown in the filtered images of w-OCP (Fig. 2L) and c-OCP (Fig. 2N) also corresponded to the edge dislocations with $\vec{b}$ = 1/3 [010] observed in the HRTEM images of these crystals (Fig. 2H, J). The filtered images as well as the HRTEM images showed the extra half planes indicating the presence of edge dislocations in the w-OCP and c-OCP crystals. The screw, mixed and edged dislocation lines can be detected by the appearance of contrast according to $\vec{g} \cdot \vec{b} = 0$, respectively, where $\vec{g}$ is reflection vector, in bright and dark filed images of TEM [41]. The presence of edge and screw dislocations was observed in size enough HA crystals [42] (more than several micrometer scale in thickness and width) to detect the contrast in terms of extinction distance. However, this observation method could not be applied to thin crystals of w-OCP and c-OCP with a thickness and width of approximately less than 50 nm and 500 nm, respectively (Fig. S1, Supplementary information).

The edge dislocation densities were estimated by filtering of the HRTEM images of w-OCP and c-OCP (Fig. S2). The total densities of edge dislocations with Burgers vectors perpendicular to the *a*-axis were 0.20 ± 0.12 × 10^{17} and 1.21 ± 0.02 × 10^{17} m^{-2} for w-OCP and c-OCP crystals, respectively (Table S1, Supplementary informa-

tion). The dislocation density ratios of the (002) per (030) were approximately 0.9 and 2.0 for the w-OCP and c-OCP crystals, respectively, which suggested that the extra half planes along the *c*-plane were easily introduced into the c-OCP crystal as compared to the w-OCP crystal. Distortion of the (002) and (030) lattice fringes in the c-OCP crystal was observed over a large region of the images (Fig. S2 I, J). Simon *et al*. reported the lattice fringes gaps (around 10 Å) indicated the presence of osteocalcin surrounded by the HA crystal using the filtered HRTEM images obtained by inverse FFT [20]. However, such a discontinuation corresponding to the estimated size of gelatin molecules in the fringe region, such as the estimated diameter of 3/2 helix α-chain (approximately 5–6 Å) [43], were not detected in the filtered images of c-OCP for both the planes (Fig. S2I, J). The granules of c-OCP contained approximately 10 wt.% of gelatin as estimated by thermogravimetric analysis (Fig. S3), which suggests that smaller number of gelatin molecules relative to the number of OCP unit cell could be present around OCP crystals not within the lattice of OCP in the basis of the calculation using the molecular weight of gelatin used in this study ($1–2 \times 10^{-3}$ mol of gelatin per 1 mol of OCP). This hypothesis was substantiated through the analysis: the lattice parameters of c-OCP estimated by Rietveld analysis indicate that the lattice of c-OCP slightly contracted rather relative to that of w-OCP (Table S3). According to the results of filtered HRTEM and Rietveld analysis, gelatin molecules could be difficult to incorporate into the lattices structure of c-OCP. Almost all of them could exist on the surface of c-OCP and the spaces in the granules. In the filtered images of the w-OCP crystals, the fringes of the (002) and (030) planes seemed to be rectilinear (Fig. S2G, H). Previously, the chemical analysis displayed that the molar ratio of Ca/P of the w-OCP and c-OCP was lower than that of stoichiometric OCP [5,8,21,30], which means that w-OCP and c-OCP crystal include point defects such as Ca^{2+} deficient sites in these crystal lattices. However, in the present study, HRTEM observations revealed unexpectedly that the synthesis process involving gelatin molecules introduced a high density of line defects, consequently inducing lattice strain in the OCP crystals.

3.2. *Characterization of c-OCP and w-OCP incubated* in vivo *and* in vitro

The w-OCP and c-OCP crystals were incubated *in vivo* and *in vitro* to examine the relationship between the structural differences of OCPs and their hydrolysis behavior for transformation into HA phases. Blight field images of TEM divulged that w-OCP and c-OCP crystals implanted into the abdominal subcutaneous pouches of the rats at 2 weeks (Fig. 3A, C). The depositions were observed as darker lines toward the long axis of the crystals and indefinite shapes on the top and side surfaces of the plate crystals, respectively, in the TEM images of both OCPs. Moreover, several similar pits were observed on the surface of the c-OCP crystal (Fig. 3C), but not on that of the w-OCP crystal (Fig. 3A). In the SAED patterns for w-OCP crystal (Fig. 3B), diffraction spots assigned to (020) plane of OCP and (020) plane of HA were detected at 4.86 and 4.07 Å, respectively. For the SAED pattern of c-OCP crystal (Fig. 3D), the spots at 3.03, 3.04 and 2.82 Å were attributed to (030) plane of OCP, $(0\bar{2}2)$ plane of OCP and $(0\bar{2}2)$ plane of HA, respectively. Furthermore, the diffraction spots at 3.4 Å in the patterns for w-OCP and c-OCP were assigned to the (002) plane of OCP and (002) plane of HA. These SAED patterns of w-OCP and c-OCP crystals indicate the reflections along the [100] zone axis, respectively, corresponding to OCP and HA crystals. These SAED pattens indicate that the line-like dark depositions were *de novo* HA crystals and the *c*-axis of the HA and OCP crystals were parallel. Previously, chemical analysis of w-OCP was performed to determine the molar ratio of Ca/P, which is an indicator of the progress of the hydrolysis, before and after the implantation at 8 weeks [34]. The molar ratio of Ca/P of the w-OCP crystal increased from 1.30 to 1.49 after the implantation [34]. In the present study, the Ca/P ratios for c-OCP, before and after the incubation were 1.30 and 1.56, respectively.

For the *in vitro* incubations, 150 mM tris-HCl buffers with an ionic strength and pH similar to the physiological conditions, and SBF with inorganic ion concentrations similar to human blood plasma [35], were applied in the present study. TEM images of the original OCPs revealed that the aspect ratio of c-OCP crystal tended to be higher than that of w-OCP crystal, which suggested that crystal growth toward the *b*-axis was suppressed by the presence of the gelatin molecules. After incubation in tris-HCl buffer, w-OCP crystals were partially dissolved from the *a*-plane on the edge of the plate (Fig. 3E). In contrast, the c-OCP crystals formed slit-like cracks on the edge of the plate at 7 days (Fig. 3F). Consequently, the formation of cracks progressed along the *c*-axis at 15 days in the buffer solution. On day 7 of the incubation, a large number of small pits were observed on the inside of the c-OCP surface (*a*-plane) compared to that of the w-OCP surface (Fig. S4). The pits appeared to be originating from the formation of cracks toward the *c*-axis inside the plate surface.

The dissolution kinetics of w-OCP and c-OCP in tris-HCl buffer was assessed by an empirical rate law [44] expressed in Eq. (1),

$$J = k_d |\sigma|^n \tag{1}$$

where k_d, and n are rate constant and effective reaction order, respectively. J and σ are dissolution rate normalized by the surface area during the dissolution and degree of relative undersaturation, respectively, which were estimated by the resulting ions composition in tris-HCl buffer incubated with OCPs (Table S4 and Fig. S8). The logarithmic plot J *versus* σ (Fig. 3G, H) displayed higher linearity for c-OCP and w-OCP dissolution in tris-HCl buffer which was undersaturated with respect to OCP at 37 °C during the incubations for 300 s. The k_d obtained from the intercept of the plot at 37 °C was 1.10×10^{-8} and 1.32×10^{-8} mol·m^{-2}·s^{-1} for w-OCP and c-OCP, respectively, under the unsaturated condition with respect to OCP. The n corresponding to the slope of the plot for w-OCP and c-OCP was 1.05 and 3.63, respectively. The tris-HCl buffer incubated with OCPs achieved almost the saturation with respect to OCP for 600 s.

Saturation generally means that a dissolution rate counterpoises deposition rate. However, OCP is converted into HA through the hydrolysis reaction through the Pi ion release because HA is more stable phase than OCP while the solution is saturated with respect to OCP [45]. The condition of human serum is also saturated with respect to OCP and supersaturated with respect to HA [46] which should have a driving force for the induction OCP hydrolysis. Thus, Pi release from OCPs was also measured in tris-HCl buffer (0.5 mM Ca^{2+} and 0.5 mM Pi ion) simulating the magnitude related to the degree of supersaturation between OCP and HA in the serum. The release amount of Pi per unit surface area of c-OCP was significantly higher than that of w-OCP with and without 5 wt.% gelatin at each incubation time (Fig. S9A, B), although there was no significant difference between w-OCP with and without gelatin molecule. The reaction rate constants for hydrolysis of w-OCP and c-OCP were determined following the chemical reaction formula as (2):

$$\frac{10}{8}Ca_8H_2(PO_4)_6 \cdot 5H_2O \rightleftharpoons Ca_{10}(PO_4)_6(OH)_2 + \frac{3}{2}H_3PO_4 + \frac{17}{4}H_2O \tag{2}$$

The slope of logarithmic plot for the concentration of remained OCP *versus* reaction rate (Fig. S9C, D and Table S5, S6) indicates that the order of hydrolysis reaction was considered as $n = 1$ for w-OCP and c-OCP. The reaction rate constants obtained from the intercept of the plot were 2.88×10^{-3} and 4.79×10^{-3} s^{-1} for w-

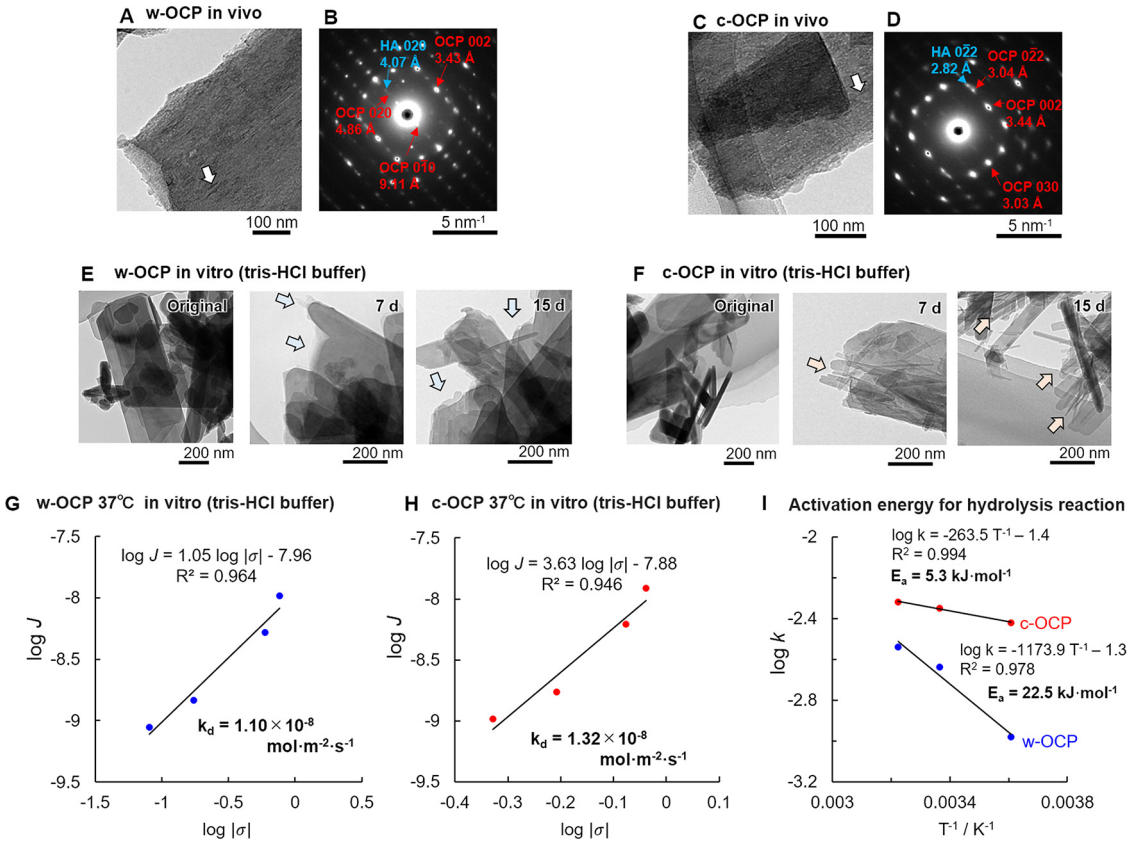

Fig. 3. Dissolution and hydrolysis of OCPs after incubation *in vivo* and *in vitro*. TEM and SAED images of w-OCP (A, B) and c-OCP (C, D) crystals after implantation in abdominal subcutaneous pouches of rats at 2 weeks. Open arrows in the TEM images indicate the *de novo* crystal formed on the w-OCP (A) and c-OCP (C) crystals along with the longer direction of the plate after implantation in rats. The SAED patterns of w-OCP (B) and c-OCP (D) crystals indicate the reflections along the [100] zone axis, respectively, corresponding to both OCP and HA crystals. TEM images of w-OCP (E) and c-OCP (F) crystals before (original) and after incubation in tris-HCl buffer at 7 and 15 days. After the incubation in the buffers, w-OCP (E) partially dissolved along the edge on the *a*-plane (blue arrows). In contrast, slit cracks toward the *c*-axis direction (orange arrows) were observed on the edge of c-OCP (F). Logarithmic plot of degree of relative unsaturation with respect to OCP *versus* dissolution rate of w-OCP (G) and c-OCP (H) incubated in tris-HCl buffer over 0–300 s. Arrhenius plots for hydrolysis reaction of w-OCP and c-OCP in tris-HCl buffer containing 0.5 mM Ca and 0.5 mM Pi ion (I).

OCP and c-OCP, respectively, at 37 °C. The activation energy, E_a, for the hydrolysis reaction was lower in c-OCP than in w-OCP (Fig. 3I).

In the present study, the surface chemical states of w-OCP and c-OCP crystals were analyzed using XPS to understand the progress of the hydrolysis reaction in tris-HCl buffer (Fig. 4), because the formation of HA by the hydrolysis was not clearly detected by X-ray diffraction (Fig. S5). In the P 2p XPS spectra, the peaks attributed to PO_4^{3-}, HPO_4^{2-}, and $H_2PO_4^{-}$ were separated at 132.6 ± 0.3, 133.6 ± 0.3, and 134.6 ± 0.3 eV, respectively, on the surface of the original and incubated OCPs through curve fitting of these spectra (Fig. 4A, B). The calculation results of the abundance ratio obtained from the integral intensities of these peaks indicate that the ratio of PO_4^{3-} increased and HPO_4^{2-} decreased on the surface of c-OCP (Fig. 4D) crystals with the incubation periods, although these ratio tended to maintain on the surface of w-OCP (Fig. 4C). The increment rates of PO_4^{3-} for c-OCP were higher than those for w-OCP in tris-HCl buffer over 0–15 days. The XPS analysis also showed that the PO_4^{3-} ratio increased on the surface of c-OCP incubated in SBF for 15 days (Fig. S6). However, the ratio of PO_4^{3-} on the surface of w-OCP tended to decrease over 7–15 days in SBF.

Based on the results of chemical analysis of OCPs implanted into rats, the hydrolysis of c-OCP was accelerated compared to that of w-OCP. The *de novo* HA crystals were formed on the w-OCP and c-OCP crystals by epitaxial growth and additional deposition on the w-OCP and c-OCP crystals placed *in vivo* (Fig. 3A–D). According to a previously proposed mechanism of the hydrolysis, the diffusion of both HPO_4^{2-} ions and water molecules in the hydrated layer of the OCP lattice occurs to induce the epitaxial growth of HA at the initial stage [47]. In addition, the dissolution–reprecipitation reaction is assumed to be involved in the additional deposition of *de novo* HA crystals. In terms of morphological changes, several studies reported that OCP crystals formed slit-like cracks along the *c*-axis formed on the edge of the *a*-plane in the buffer under the control of the addition of Ca^{2+} [48] or solution temperature [49]. Iijima *et al.* especially reported that the cracks were formed through the diffusion of water molecules from the OCP lattice during the transformation into HA [48]. The c-OCP crystals completely cracked toward the *c*-axis direction in tris-HCl buffer at 15 days (Fig. 3F). This also relates to that the behavior of the dissolution and subsequent hydrolysis was different for c-OCP and w-OCP crystals. The effective reaction orders suggest that surface diffusion and surface-pit formation [50,51] control the dissolution of w-OCP and c-OCP, respectively. The surface pits observed by TEM strongly supports the dissolution mechanism of c-OCP estimated by the empirical rate law. Furthermore, the pits initiated the formation of slit from the inside of *a*-plane of c-OCP commonly in the buffer and *in vivo* environment (Fig. S4). In the dissolution of minerals, the strain around the dislocation core reduces the energy barrier for the nucleation of pits [52]. Thus, the formation of pits could be a typical process to promote the hydrolysis of c-OCP including the higher density of dislocation.

In the present study, the rate of the dissolution and hydrolysis reaction of w-OCP and c-OCP were examined *in vitro*. The

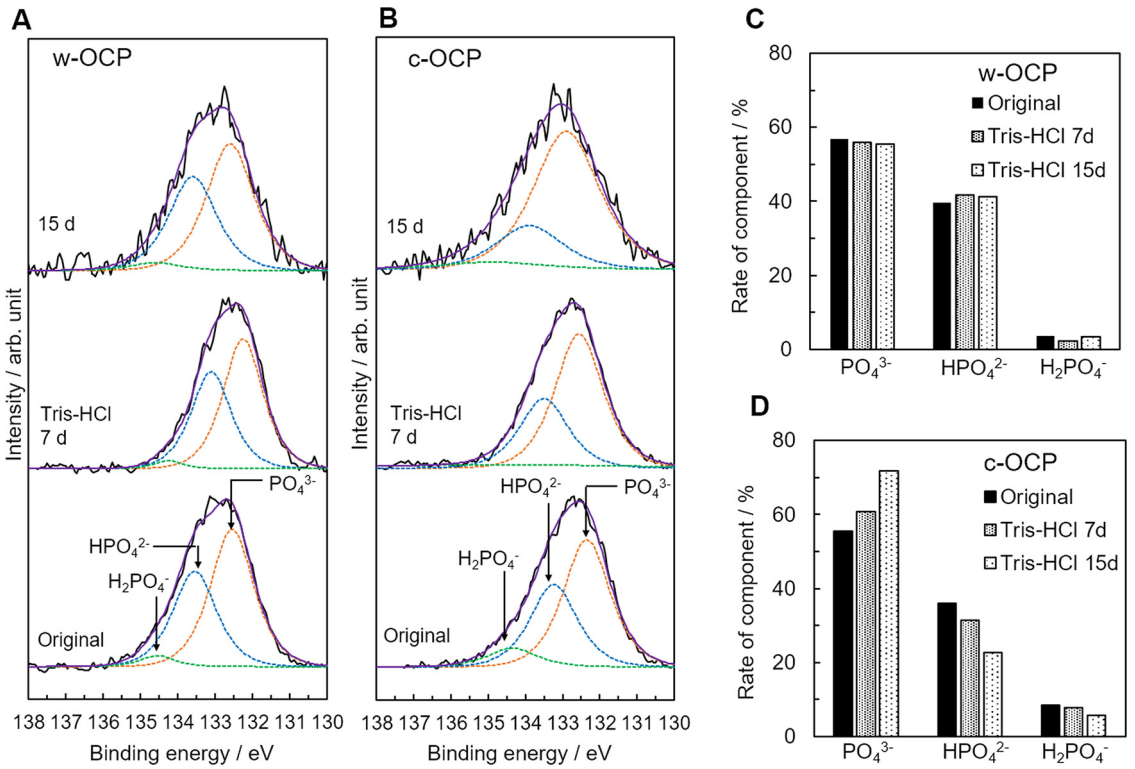

Fig. 4. Surface hydrolysis of OCPs and state of remaining gelatin on c-OCP after incubation *in vitro*. Narrow P 2p XPS spectra of w-OCP (A) and c-OCP (B) crystals before (original) and after incubation in tris-HCl buffer at 7 and 15 days. Rates of components of phosphate species on the surface of w-OCP (C) and c-OCP (D) crystals before (original) and after the incubation in tris-HCl, which was calculated by the integral intensities of separated peaks in the P 2p XPS spectra.

value of decrement in E_a from w-OCP to c-OCP was approximately 17 kJ·mol^{-1} for the hydrolysis reaction through the diffusion of Pi ions (Fig. 3I). Activation energy of chemical reaction can be reduced by not only a presence of catalysis but also increment of internal energy of reactant. The strain accumulation by increasing the dislocation density leads the increment of internal energy of reactant [53]. The energy increment induced by incorporation of edge dislocation, ΔE_{dis}, is estimated by dislocation density [53] and self-energy of dislocation depending on the magnitude of Burgers vector [41]. The calculated ΔE_{dis} for c-OCP was approximately 3 times higher than that for w-OCP (Table S2), indicating that the introduction of edge dislocations into c-OCP decreased E_a compared to w-OCP. If the elastic modulus and Poisson's ratio are assumed to be 60–80 GPa and 0.28, respectively, based on these reported values of ACP and CDHA [54–56], the value of increment in ΔE_{dis} from w-OCP to c-OCP was estimated to be 16–21 kJ·mol^{-1} (Table S2), which was similar to the scale of E_a decrement in the hydrolysis reaction. However, it is also considered that the mismatch between the increment values of ΔE_{dis} and the decrement of E_a in c-OCP compared to w-OCP could be caused by inhibiting Pi ion release due to the adsorption of gelatin onto c-OCP (Figs. S7, S9).The presence of mixed dislocations, which were unable to observe both in the HRTEM and filtered images, also may be a factor in the mismatch of energy differences. The mixed edge dislocations exhibit lower self-energy than edge dislocation [41]. According to Arrhenius law, the higher dissolution rate constant of c-OCP in condition of undersaturation with respect to OCP (Fig. 3G, H) indicates that the increment of ΔE_{dis} by the dislocation could also contribute to the promotion of c-OCP dissolution due to decreasing the activation energy. Focused on the surface chemical state, the increase in PO_4^{3-} and decrease in HPO_4^{2-} analyzed by XPS (Fig. 4A–D) support that hydrolysis of c-OCP through the dissolution and subsequent diffusion progressed faster than w-OCP crystal did on these crystal surfaces in tris-HCl buffer. The XPS analysis for the crystal incubated in SBF also suggests that c-OCP has a higher activity in inducing the hydrolysis reaction (Fig. S6) although SBF is supersaturated with respect to OCP as well as HA. Taken together, it is probable that the higher density of edge dislocation is associated with the acceleration of dissolution of OCP and its subsequent hydrolysis reaction with the diffusion, resulting in that the c-OCP transforms into HA faster compared to w-OCP in physiological conditions *in vivo* and *in vitro*.

3.3. Analysis of new bone formation and bone quality induced by OCPs/Gel disks in rat calvarial defects

Although the bone formation capacity of OCP materials implanted in bone defects can be directly compared using the granule forms of OCP [5,8,37,57], the composite forms of w-OCP and c-OCP crystals with gelatin sponge (w-OCP/Gel and c-OCP/Gel disks, respectively) were used to ensure stable handling during implantation (Fig. S10), thereby obtaining a new bone volume comparable to that reported in previous studies [31–33,36,58]. The results of the radiographic observation of the implantation of 46% (weight percent) c-OCP/Gel and 46% w-OCP/Gel disks in rat calvaria at 8 weeks are shown in Fig. 5A. Both implants showed radiopacities; however, 46% c-OCP/Gel had a higher radiopacity, to some extent even in the area close to the superior sagittal sinus than the 46% w-OCP/Gel. Slight radiopacity was observed along the defect margin in the control (no implantation) group. Histological sections of the rat calvarial defects supported the radiopacity results that the newly formed bone by 46% c-OCP/Gel almost occupied the defect (Fig. S11), thus suggesting replacement with substantial amount of new bone after almost complete material biodegradation. In contrast, although the new bone was well formed by 46% w-OCP/Gel, it was apparent that some of the w-OCP granules remained unresorbed. These tendencies were identical to the histomorphometric findings for the percentage of newly formed bone in the defect (n-

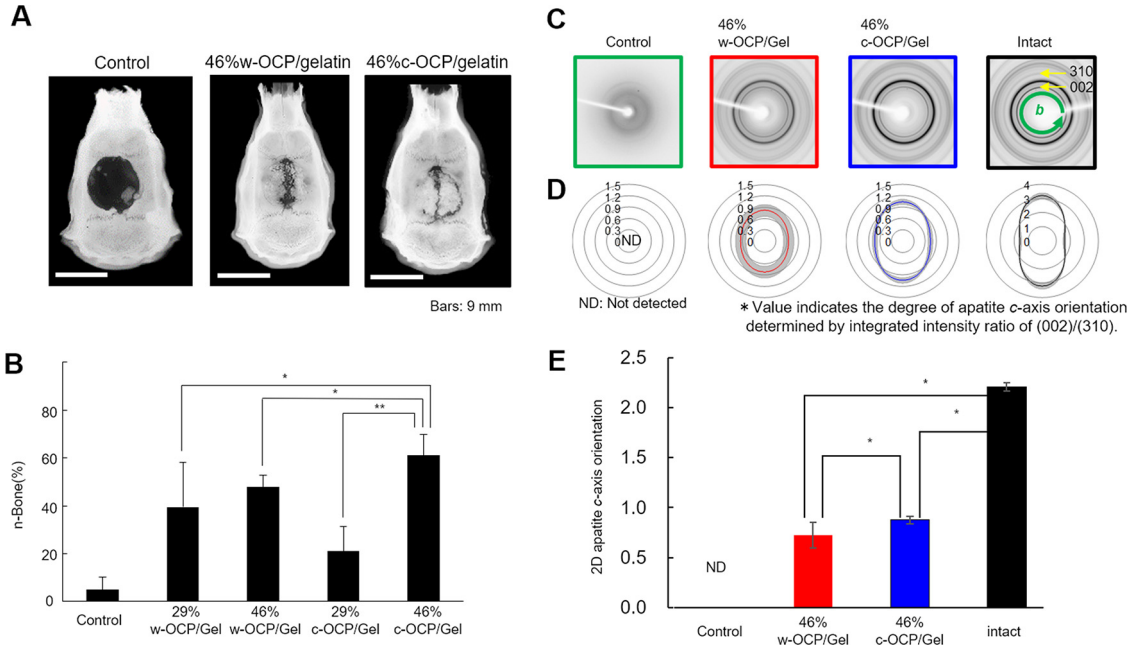

Fig. 5. Histomorphometry of new bone formation and microbeam X-ray diffraction analysis of bone apatite crystal orientation in the area of bone regeneration. (A) Soft X-ray images at 8 weeks after the implantation. (B) Newly formed bone% (n-Bone%) ($^{*}p < 0.05$, $^{**}p < 0.01$, $n = 5$, error bars on the plot correspond to SD.). (C) Debye ring images from which the diffracted intensity from (002) and (310) planes of apatite were analyzed. (D) Radar chart showing 2D distribution of apatite *c*-axis orientation along the calvaria surface in which the gray-hatched ranges indicate SD. (E) Degree of 2D apatite *c*-axis orientation along the calvaria surface determined through the integration of X-ray intensity distribution ($^{*}p < 0.05$, $n = 5$, error bars on the plot correspond to SD.). Control indicates negative control group with no implantation in the calvarial defect.

Bone%). The 46% c-OCP/Gel enhanced new bone formation more than the one with lower c-OCP content (29%) or w-OCP/Gels comprising 29 and 46% of w-OCP (Fig. 5B).

The crystallographic orientation of bone apatite *c*-axis in new bone matrices as an important bone quality index reflecting bone mechanical integrity [59,60], was quantitatively analyzed using a microbeam X-ray diffractometer system (Fig. 5C–E). The results presented that although the preferential orientation was highest in intact rat calvarial bone, the orientation of apatite induced by the implantation of 46% c-OCP/Gel was significantly higher than that of 46% w-OCP/Gel according to the radar diagrams determined by the integrated intensity ratio of (002) / (310) (Fig. 5D) and by 2D apatite *c*-axis orientation in rat calvaria. No diffraction peak was detected in the control group (no implantation), suggesting that OCP/Gel implantation enhances not only the bone formation, but also the preferential apatite *c*-axis orientation, particularly, c-OCP/Gel implantation. This was identical to the histological evidence that the bone regeneration caused by 46% c-OCP/Gel was matured, showing a lamellar structure throughout the defect without the remnants of c-OCP granules, whereas, that caused by 46% w-OCP/Gel was not sufficiently ordered and exhibited some connective tissues and the remnants of w-OCP granules (Fig. S11).

3.4. Cell culture experiments

Capacities to stimulate osteoblastic differentiation were examined by 2D cultures of mouse bone marrow-derived MSC line D1 (Fig. 6A). ALP activity, which is an earlier osteoblastic differentiation marker, was determined on each day of incubation. The effect of gelatin molecules on the cellular activity was also investigated in the culture. The cells were incubated in the presence of w-OCP and 10 wt.% of gelatin. The concentration of gelatin was determined by referencing the gelatin content in c-OCP which was estimated by thermogravimetric analysis (Fig. S3). Considering that the gelatin on c-OCP could be partially desorbed from the crystal surface in the physiological condition (Fig. S7), the incubation with w-OCP in the presence of 5 wt.% gelatin was also carried out. The D1 cells incubated with w-OCP and w-OCP + gelatin as well as c-OCP achieved the highest ALP activities in the 2D culture at day 14 (Fig. 6A). The activity of c-OCP group was significantly higher than that of w-OCP and w-OCP + gelatin groups at day 14, whereas there was no significant difference between these groups at days 7. The activity of D1 cells incubated with c-OCP significantly decreased compared to control and w-OCP regardless of the presence of gelatin at day 21. However, the activities tended to decrease with increasing the amount of gelatin on w-OCP during the incubations over days 7 to 21.

Moreover, 3D cultures of D1 cells with c-OCP and w-OCP were performed in this study. D1 cell spheroids incorporating the w-OCP and c-OCP crystals (Fig. 6B) were formed on the cell culture chips. The diameters of the D1/w-OCP and D1/c-OCP spheroids were approximately 316 and 250 μm, respectively, which was larger than that of the D1 cell-only spheroids (133 μm) on day 6. The cell proliferation of the D1/w-OCP and D1/c-OCP groups significantly increased compared to the D1 cell-only groups for each period (Fig. S12). The D1/w-OCP and D1/c-OCP spheroids in the 3D cultures showed the highest ALP activity at day 14 in common with the 2D cultures (Fig. 6C). The ALP activity of the D1/c-OCP spheroids was significantly higher than that of the D1/w-OCP spheroids, although the activity of D1/c-OCP was lower than that of D1/w-OCP at day 7.

The spectroscopic characteristics of OCP crystals collected from the spheroids after incubation was also analyzed using FT-IR and Raman spectroscopy (Fig. 6D, S13). The characteristic OCP peaks corresponding to the ν_3 PO_4 and ν_3 HPO_4 stretching mode at 1075 cm^{-1} and ν_3 PO_4 stretching mode at 1035 cm^{-1} clearly appeared in the FT-IR spectra for both OCP until incubation at day 7 (Fig. 6D). However, the intensities of these peaks decreased in the spectra of c-OCP compared to that of w-OCP at day 14 of the incubation. At day 21, the peaks for the incubated w-OCP appeared broad, similar to those of c-OCP. The decrease in the intensity in FT-IR spectra was related to the hydrolysis of OCP *in vivo* [34] and

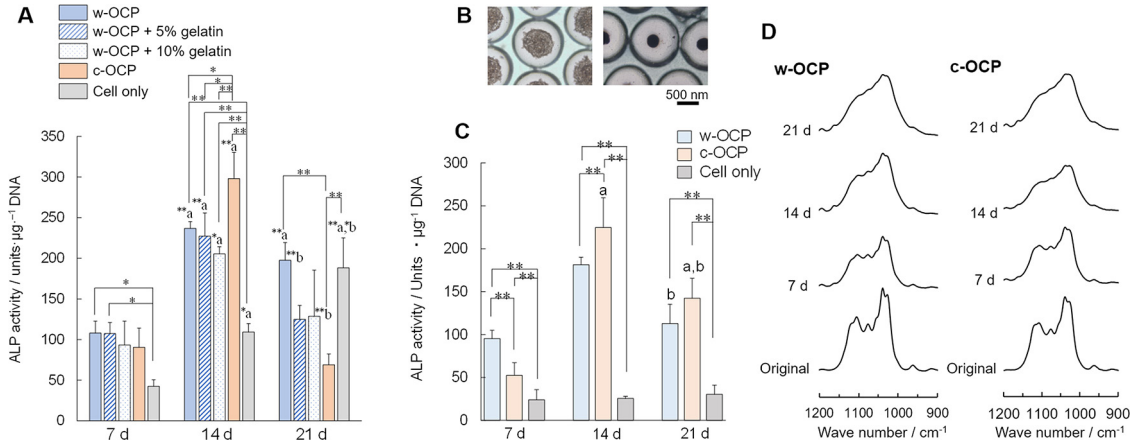

Fig. 6. Osteoblastic differentiation of MSC and hydrolysis of OCPs in 2D and 3D culture. ALP activity (A) of the D1 cell-only (control) and cells incubated with w-OCP, w-OCP + 5% gelatin, w-OCP + 10% gelatin as well as c-OCP after 7, 14, and 21 days of 2D culture ($^{*}p < 0.05$ and $^{**}p < 0.01$, significant difference among groups at each day of culture, $^{**a}p < 0.01$ from 7 days, $^{*a}p < 0.05$ from 7 days, $^{**b}p < 0.01$ from 14 days, $^{*b}p < 0.05$ from 14 days of incubation in each group, $n = 3$, error bars on the plot correspond to SD.). Light microscopy images of D1 cell after seeding (left side) and incubation after 6 days (right side) on the 3D cell culture chips with the presence of the c-OCP granules (B). ALP activity (C) of the D1 cell-only (control) spheroids, D1/w-OCP and D1/c-OCP spheroids after 7, 14 and 21 days of 3D culture ($^{*}p < 0.05$ and $^{**}p < 0.01$, significant difference among groups at each day of culture, $^{a}p < 0.01$ from 7 days, $^{b}p < 0.01$ from 14 days, $^{c}p < 0.05$ from 7 days of incubation in each group, $n = 6$, error bars on the plot correspond to SD.). FT-IR (D) of w-OCP and c-OCP crystals before (original) and after incubation in the spheroids at 7, 14 and 21 days.

in vitro including the cell culture conditions [37]. The intensity of ν_1 HPO_4 decreased for c-OCP relative to w-OCP in the Raman spectra at day 14, which also indicates the progress of the hydrolysis reaction (Fig. S13).

In the present study, the *DS* with respect to HA and OCP was determined by the measurement of ion concentration and pH in the culture environments (Fig. S14). The *DS* values with respect to HA and OCP were in the order of 10^{13}–10^{16} and 10^{4}–10^{6}, respectively, which indicated that the culture medium was supersaturated with respect to HA and OCP for all groups during the incubations. The *DS* with respect to HA and OCP increased until day 4 and subsequently decreased from day 6 to day 20 for all the groups. Focusing on the *DS* values with respect to HA, while the ALP activities of D1/OCPs spheroids increased from day 7 to day 14, the culture medium incubated with D1/c-OCP spheroids was more supersaturated with respect to HA relative to D1/w-OCP spheroids from day 6 to day 14.

4. Discussion

Mathew *et al.* reported that OCP can be composed of a non-stoichiometric chemical composition with $Ca_{16}H_{4+X}(PO_4)_{12}(OH)_X{\cdot}(10\text{-}X)H_2O$ [17]. It is also known that the Ca/P molar ratio of OCP varies from 1.23 to 1.37 *versus* the stoichiometric ratio of 1.33 [8,21,61], which means that some of the OCPs include point defects in their lattices. The present study revealed through the lattice image analyses by HRTEM and FFT that both c-OCP and w-OCP crystals were identical to the reported OCP structure without containment of other phases, such as the amorphous phase [62]. However, c-OCP crystal had an edge dislocation and a strain in the structure, most probably introduced during wet preparation in the presence of gelatin molecules. The present study showed that the presence of gelatin increased the crystal length but inhibited the crystal width in OCP when observed by scanning electron microscope (SEM) (Figs. S1 and S10C, F). A previous study showed that the length of the crystal along the *c*-axis of c-OCP was over two times longer than that of w-OCP, indicating that gelatin can interact with specific planes of OCP crystals [33,63]. Although the morphology of c-OCP could be regulated through a relatively strong interaction with *a*-plane during the crystal growth, the present study suggested that the dislocation (line defect) could be introduced via a weak interaction between gelatin molecules and the *b*-plane of OCP during crystal growth.

Filtering the HRTEM images carried out by masking the FFT spots corresponding to the crystal planes along the *b* and *c*-planes in the OCPs disclosed that edge dislocations were present in the c-OCP crystal under the higher density (Table S1). Gelatin molecules were detected on the surface of c-OCP crystals (Figs. S3 and S7) and were present even after soaking in tris-HCl buffer (Fig. S7). A structural model explaining a weak interaction can be successfully considered between hydroxyproline of gelatin and *b*-plane of phosphate groups in the c-OCP structure based on structural considerations (Fig. S15). A plausible mechanism introducing dislocation is: (1) the increase in the differential stacking rate of OCP-like cluster between the *c*-axis and *b*-axis directions caused by gelatin adsorption onto the *b*-plane of c-OCP (higher growth toward *c*-axis than *b*-axis); (2) possible step formation on the growth front of nanoparticles composed of the assembled OCP-like clusters according to the distinct growth rate; and (3) introduction of the dislocation starting from the step when the nanoparticles are attached each other toward the *c*-axis (Fig. S15).

Collected data of OCP materials, including c-OCP as a bone-substitute material [4,5,31–33,57,58] suggest that accelerated biodegradation is the most prominent characteristic of c-OCP. Although OCP is usually resorbed via osteoclastic cellular phagocytosis mechanism, for both c-OCP or w-OCP, regardless of the presence of biopolymers such as gelatin as composite matrices [8,31], c-OCP can be replaced with a new bone via its complete biodegradation in rat calvaria [31] and rabbit tibia standardized defects [32] under the condition that w-OCP or a highly porous rapid resorbable material, β-tricalcium phosphate (β-TCP), is not completely resorbed [5,32]. The present study further highlighted one of the most significant performances of c-OCP that the rapid resorption finally leads to the acquisition of a new bone with higher bone quality characterized by apatite *c*-axis orientation (Fig. 5D, E). The biomaterial performance can be explained by a specific mechanism involving c-OCP enhancing (1) the crystal dissolution and Pi ion release relating hydrolysis originating from the introduced edge dislocation (Fig. 3G, H and Fig. S9) and (2) the conversion to HA crystals (Fig. 7), as observed in the crystal dissolution (Fig. 3E–H) and the surface hydrolysis in tris-HCl buffer (Fig. 4), or in the formation of new deposits on the crystal surfaces in rat subcutaneous tissues (Fig. 3A–D) and the surface hydrolysis in SBF (Fig.

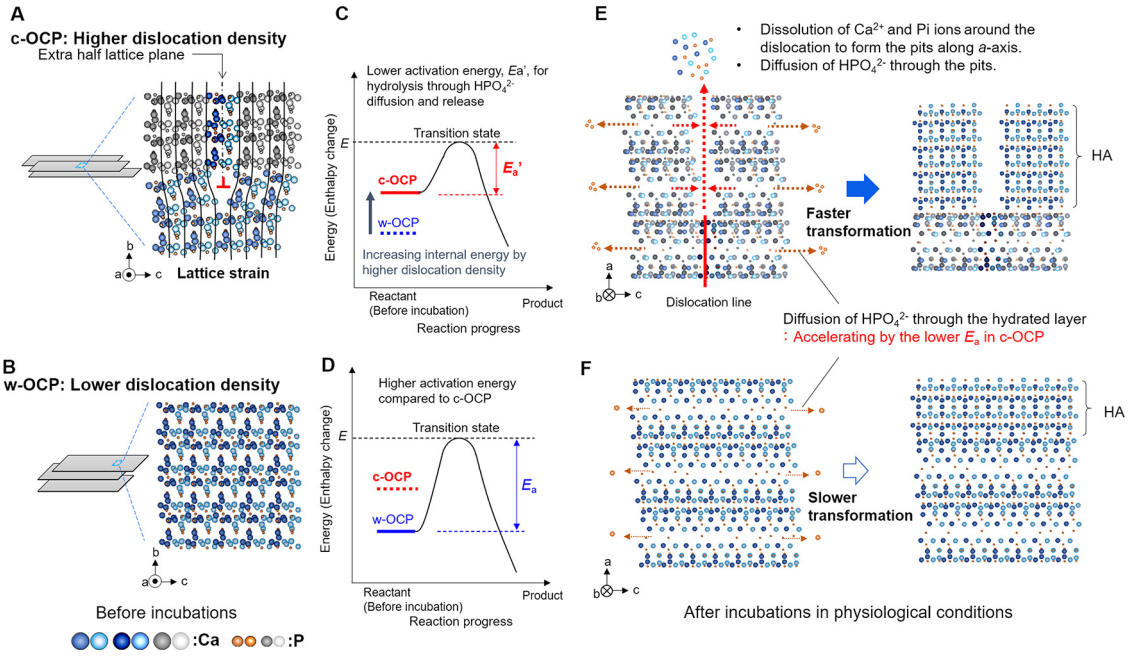

Fig. 7. Proposed mechanism for promoting the hydrolysis of c-OCP under physiological conditions. Schematic images of the structure of *c*-plane on c-OCP and w-OCP crystals before incubation (A, B). The (002) plane of c-OCP (A) includes larger number of the edge dislocations having Burgers vector perpendicular to *a*-axis relative to w-OCP. The *b*-plane of OCP also includes the dislocations. Lattice strain is induced around the sites of the edge dislocations. Schematic diagrams of energy transition for c-OCP (C) and w-OCP (D) regarding dissolution and hydrolysis through the HPO_4^{2-} diffusion in physiological condition. Increasing the internal energy by the higher dislocation density reduces activation energy for the reaction for c-OCP compared to w-OCP. Process of hydrolysis reaction of c-OCP (E) and w-OCP (F) crystals in physiological environment. HPO_4^{2-} ions diffuse in hydrated layer toward the *c*- and *b*-axis direction of c-OCP (E) and w-OCP (F) crystals. The higher dislocation density accelerates the diffusion of HPO_4^{2-} in c-OCP due to decreasing activation energy for the hydrolysis, resulting in faster transformation of c-OCP into HA compared to w-OCP. The pits along *a*-axis are formed at the edge dislocation sites on c-OCP, because the lattice strain around the dislocation core decreases the energy barrier for the nucleation of pit. The formation of pits on the c-OCP crystal could become the additional paths for the HPO_4^{2-}diffusions along *a*-axis, resulting in promoting the hydrolysis of c-OCP.

S6). These chemical changes were also supported by the increase of Ca/P molar ratio in rat subcutaneous implantation and phase transformation toward HA in a 3D culture condition, as supported by the Raman spectra (Fig. S13) and the change in *DS* in the culture media with respect to HA and OCP (Fig. S14). A plausible mechanism for dissolution and subsequent hydrolysis associated with a structure specific to c-OCP was proposed (Fig. 7). The main possible mechanism is that the higher dislocation density in c-OCP reduces the activation energy for the HPO_4^{2-} diffusion along the *c*- and/or *b*-axis direction from the hydrated layer, accelerating the hydrolysis of c-OCP and epitaxial HA growth. The dissolution rate of c-OCP could be increased through the formation of large number of pits around the edge dislocations from the surface, when a higher density is introduced in c-OCP beyond the density of w-OCP along the *a*-axis direction. Thus, the pits act as the enhancer from the side that HPO_4^{2-} is diffused together with the path through the hydrated layer in the OCP structure, contributing the enhancement of the whole hydrolysis.

The precise mechanism of bone regeneration by OCP is of general interest not only in biomaterials science, but also in bone physiology because of its possible role as an apatite precursor in bone mineralization [22,64–68]. The present *in vitro* and *in vivo* analyses substantiated a relation between the materials property and cellular/tissue reactions that the lattice dislocation-dependent dissolution process of c-OCP, in addition to the known hydrated layer ion diffusion, is in essence involved in enhancing MSC differentiation toward osteoblasts and bone regeneration in the experimentally created defects (Figs. 5 and 6). A previous study found that the estimation of ALP activity of 3D MSC spheroid culture with calcium phosphate materials, including OCP, as observed in the present study, can be correlated with *in vivo* bone formation capacity [37]: the increase of osteoconductivity of OCP through the structural and chemical modification found in the present c-OCP may have a clinical relevance. The results of implantation of OCPs with the gelatin matrices into the bone defect and 2D culture of w-OCP in the presence of gelatin molecules suggest that the gelatin pre-present on the surface of c-OCP has limited influence on the differentiation of MSC into osteoblast and new bone formation. This also supports that the effect of the distinct dissolution and the hydrolysis of c-OCP is surely reflected in the bone regeneration. The relation between the incorporation of dislocation at higher density and the acceleration of dissolution/ hydrolysis of OCP was verified by the kinetic analysis *in vitro*. In particular, the increment of internal energy at the higher dislocation density is associated with the decrement of activation energy for the hydrolysis reaction (Fig. 3I and Table S2). The acceleration of pit formation around the dislocation in c-OCP was in agreement with the morphological changes observed by TEM and the analysis using the empirical rate law (Figs. 3E–H and S4). The fact that the lattice did not expand in c-OCP crystals indicates that the gelatin molecules are not inserted in the crystal structure of OCP, which was confirmed by Rietveld analysis (Table S3). The lattice fringe gaps corresponding to the site embedding gelatin molecules in the crystals were not observed by the filtered HRTEM images of c-OCP (Fig. S2). These analyses also support that the pits could not be formed by the elution of gelatin but originated from the edge dislocations in the c-OCP crystal. These results indicate that the increase in energy instability due to the lattice strain around dislocations in higher density induces the enhancement of dissolution and hydrolysis in common. The fundamental reason for bringing about the ion release from c-OCP, which is involved in inducing distinct bone regeneration, is interpreted as the acceleration of dissolution and hydrolysis due to the incorporation of edge dislocation, where the strain was introduced during c-OCP preparation with gelatin molecules.

Similar mechanisms regarding the dissolution have been reported to arise from the pit formed within the grain boundary and edge dislocation of sintered HA ceramics [69] and propagate along the dislocation line [70]. The present results suggest that the incorporation of dislocation is surely associated with the progress of epitaxial phase transformation of calcium phosphate, taking place even under a physiological condition containing equilibrium concentration of Ca^{2+} and Pi ion with respect to OCP phase, through increasing the total energy from throughout the OCP crystal. The dislocation density in c-OCP was 10^2–10^5 times higher than that in HA regardless of doping some ions [42,71]. The line defects are categorized as edge, screw or mixed dislocation. The FFT analysis of w-OCP and c-OCP identified that the presence of gelatin in OCP preparation has an effect on incorporating the defect more as edge dislocation. The self-energy of edge dislocation is approximately 1.5 times higher compared to screw dislocation if the parameters for the calculation of energy are the same between these dislocations [41]. This estimation suggests that the gelatin molecules act as one of key additives for introducing the dislocation followed by the increment of internal energy in OCP crystal.

5. Conclusion

The results presented herein indicate that c-OCP is more chemically unstable, soluble, and capable of augmenting its bioactivity and inducing bone induction through acceleration of hydrolysis into HA compared to w-OCP. Thus, the performance of these two biomaterials is essentially distinct. The local introduction of the dislocation and strain into the OCP was essential in acquiring the materials property of OCP, in which the involvement of gelatin molecules in the preparation is indispensable. This study displayed a strategy for obtaining active biomaterials that can be extended to other functional materials in a wide range of aspects in the fields of chemical and materials science.

Data availability

All data are included in the manuscript and supplementary information appendix.

Declaration of Competing Interest

The authors declare no conflict of interest.

CRediT authorship contribution statement

Ryo Hamai: Investigation, Validation, Formal analysis, Methodology, Writing – original draft, Writing – review & editing. **Susumu Sakai:** Investigation, Validation, Writing – review & editing. **Yukari Shiwaku:** Validation, Writing – review & editing. **Takahisa Anada:** Validation, Writing – review & editing. **Kaori Tsuchiya:** Investigation, Writing – review & editing. **Takuya Ishimoto:** Investigation, Validation, Writing – review & editing. **Takayoshi Nakano:** Investigation, Validation, Writing – review & editing. **Osamu Suzuki:** Validation, Methodology, Writing – original draft, Writing – review & editing, Conceptualization, Project administration.

Acknowledgments

This study was supported in part by MEXT/JSPS KAKENHI Grant Nos. JP23106010, JP18H02981, JP18H05254, and JP21H03121. We thank Noboru Akao and Yukie Ohira for providing technical support with the XPS analysis (Instrumental Analysis Group, Graduate School of Engineering, Tohoku University) and Takamichi Miyazaki (Instrumental Analysis Group, Graduate School of Engineering, Tohoku University) for providing technical support with the TEM observations.

Supplementary Materials

Supplementary material associated with this article can be found, in the online version, at doi:10.1016/j.apmt.2021.101279.

References

[1] K. Yokoyama, M. Tomita, J. Sakai, Hydrogen embrittlement behavior induced by dynamic martensite transformation of Ni–Ti superelastic alloy, Acta Mater. 57 (2009) 1875–1885, doi:10.1016/j.actamat.2008.12.030.
[2] E. Bres, J. Barry, J. Hutchison, A structural basis for the carious dissolution of the apatite crystals of human tooth enamel, Ultramicroscopy 12 (1983) 367–371, doi:10.1016/0304-3991(83)90250-4.
[3] A. Matsugaki, G. Aramoto, T. Nakano, The alignment of MC3T3-E1 osteoblasts on steps of slip traces introduced by dislocation motion, Biomaterials 33 (2012) 7327–7335, doi:10.1016/j.biomaterials.2012.06.022.
[4] T. Kawai, S. Kamakura, K. Matsui, M. Fukuda, H. Takano, M. Iino, S. Ishikawa, H. Kawana, T. Soma, E. Imamura, H. Kizu, A. Michibata, I. Asahina, K. Miura, N. Nakamura, T. Kibe, O. Suzuki, T. Takahashi, Clinical study of octacalcium phosphate and collagen composite in oral and maxillofacial surgery, J. Tissue Eng. 11 (2020) 2041731419896449, doi:10.1177/2041731419896449.
[5] O. Suzuki, S. Kamakura, T. Katagiri, M. Nakamura, B. Zhao, Y. Honda, R. Kamijo, Bone formation enhanced by implanted octacalcium phosphate involving conversion into Ca-deficient hydroxyapatite, Biomaterials 27 (2006) 2671–2681, doi:10.1016/j.biomaterials.2005.12.004.
[6] O. Suzuki, M. Nakamura, Y. Miyasaka, M. Kagayama, M. Sakurai, Bone formation on synthetic precursors of hydroxyapatite, Tohoku J. Exp. Med. 164 (1991) 37–50, doi:10.1620/tjem.164.37.
[7] H. Imaizumi, M. Sakurai, O. Kashimoto, T. Kikawa, O. Suzuki, Comparative study on osteoconductivity by synthetic octacalcium phosphate and sintered hydroxyapatite in rabbit bone marrow, Calcif. Tissue Int. 78 (2006) 45–54, doi:10.1007/s00223-005-0170-0.
[8] N. Miyatake, K.N. Kishimoto, T. Anada, H. Imaizumi, E. Itoi, O. Suzuki, Effect of partial hydrolysis of octacalcium phosphate on its osteoconductive characteristics, Biomaterials 30 (2009) 1005–1014, doi:10.1016/j.biomaterials.2008.10.058.
[9] S. Saito, R. Hamai, Y. Shiwaku, T. Hasegawa, S. Sakai, K. Tsuchiya, Y. Sai, R. Iwama, N. Amizuka, T. Takahashi, O. Suzuki, Involvement of distant octacalcium phosphate scaffolds in enhancing early differentiation of osteocytes during bone regeneration, Acta Biomater. 129 (2021) 309–322, doi:10.1016/j.actbio.2021.05.017.
[10] O. Suzuki, S. Kamakura, T. Katagiri, Surface chemistry and biological responses to synthetic octacalcium phosphate, J. Biomed. Mater. Res. Part B 77 (2006) 201–212, doi:10.1002/jbm.b.30407.
[11] R. Nishikawa, T. Anada, R. Ishiko-Uzuka, O. Suzuki, Osteoblastic differentiation of stromal ST-2 cells from octacalcium phosphate exposure via p38 signaling pathway, Dent. Mater. J. 33 (2014) 242–251, doi:10.4012/dmj.2013-226.
[12] M. Takami, A. Mochizuki, A. Yamada, K. Tachi, B. Zhao, Y. Miyamoto, T. Anada, Y. Honda, T. Inoue, M. Nakamura, O. Suzuki, R. Kamijo, Osteoclast differentiation induced by synthetic octacalcium phosphate through receptor activator of NF-κB ligand expression in osteoblasts, Tissue Eng. Part A 15 (2009) 3991–4000, doi:10.1089/ten.TEA.2009.0065.
[13] Y. Sai, Y. Shiwaku, T. Anada, K. Tsuchiya, T. Takahashi, O. Suzuki, Capacity of octacalcium phosphate to promote osteoblastic differentiation toward osteocytes *in vitro*, Acta Biomater. 69 (2018) 362–371, doi:10.1016/j.actbio.2018.01.026.
[14] J.L. Meyer, E.D. Eanes, A thermodynamic analysis of the secondary transition in the spontaneous precipitation of calcium phosphate, Calcif. Tissue Res. 25 (1978) 209–216, doi:10.1007/bf02010771.
[15] W.E. Brown, Crystal growth of bone mineral, Clin. Orthop. Relat. Res. 44 (1966) 205–220.
[16] W.E. Brown, J.P. Smith, J.R. Lehr, A.W. Frazier, Octacalcium phosphate and hydroxyapatite: crystallographic and chemical relations between octacalcium phosphate and hydroxyapatite, Nature 196 (1962) 1050–1055, doi:10.1038/1961050a0.
[17] M. Mathew, W.E. Brown, L.W. Schroeder, B. Dickens, Crystal structure of octacalcium bis(hydrogenphosphate) tetrakis(phosphate)pentahydrate, $Ca_8(HPO_4)_2(PO_4)_4{\cdot}5H_2O$, J. Crystallogr. Spectrosc. Res. 18 (1988) 235–250, doi:10.1007/BF01194315.
[18] D.R. Simpson, Problems of the composition and structure of the bone minerals, Clin. Orthop. Relat. Res. 86 (1972) 260–286, doi:10.1097/00003086-197207000-00039.
[19] C. Rey, C. Combes, What bridges mineral platelets of bone? BoneKEy Rep. 3 (2014) 1–2, doi:10.1038/bonekey.2014.81.
[20] P. Simon, D. Grüner, H. Worch, W. Pompe, H. Lichte, T. El Khassawna, C. Heiss, S. Wenisch, R. Kniep, First evidence of octacalcium phosphate@osteocalcin nanocomplex as skeletal bone component directing collagen triple–helix nanofibril mineralization, Sci. Rep. 8 (2018) 13696, doi:10.1038/s41598-018-31983-5.
[21] O. Suzuki, H. Yagishita, T. Amano, T. Aoba, Reversible structural changes of octacalcium phosphate and labile acid phosphate, J. Dent. Res. 74 (1995) 1764–1769, doi:10.1177/00220345950740110801.
[22] W.J. Habraken, J. Tao, L.J. Brylka, H. Friedrich, L. Bertinetti, A.S. Schenk, A. Verch, V. Dmitrovic, P.H. Bomans, P.M. Frederik, J. Laven, P. van der Schoot, B. Aichmayer, G.de With, J.J. DeYoreo, N.A.J.M. Sommerdijk, Ion-association complexes unite classical and non-classical theories for the biomimetic nu-

cleation of calcium phosphate, Nat. Commun. 4 (2013) 1507, doi:10.1038/ncomms2490.
[23] W.E. Brown, J.R. Lehr, J.P. Smith, A.W. Frazier, Crystallography of octacalcium phosphate, J. Am. Chem. Soc. 79 (1957) 5318–5319, doi:10.1021/ja01576a068.
[24] H. Newsely, Darstellung von "Oktacalciumphosphat"(Tetracalciumhydrogentrisphosphat) durch homogene kristallisation, Monatsh. Chem. 91 (1960) 1020–1023, doi:10.1007/BF00899825.
[25] E. Hayek, Die mineralsubstanz der knochen, Klin. Wochenschr. 45 (1967) 857–863, doi:10.1007/BF01745681.
[26] Y. Liu, R. Shelton, J. Barralet, Homogeneous octacalcium phosphate precipitation: effect of temperature and pH, Key Eng. Mater. 254-256 (2003) 79–82, doi:10.4028/www.scientific.net/KEM.254-256.79.
[27] M. Iijima, H. Kamemizu, N. Wakamatsu, T. Goto, Y. Doi, Y. Moriwaki, Effects of Ca addition on the formation of octacalcium phosphate and apatite in solution at pH 7.4 and at 37°C, J. Cryst. Growth 193 (1998) 182–188, doi:10.1016/S0022-0248(98)00455-2.
[28] A. Bigi, B. Bracci, S. Panzavolta, M. Iliescu, M. Plouet-Richard, J. Werckmann, D. Cam, Morphological and structural modifications of octacalcium phosphate induced by poly-L-aspartate, Cryst. Growth Des. 4 (2004) 141–146, doi:10.1021/cg034078d.
[29] J. Moradian-Oldak, M. Iijima, N. Bouropoulos, H.B. Wen, Assembly of amelogenin proteolytic products and control of octacalcium phosphate crystal morphology, Connect. Tissue Res. 44 (2003) 58–64, doi:10.1080/03008200390152106.
[30] K. Tsuchiya, R. Hamai, S. Sakai, O. Suzuki, Comparative analysis of bovine serum albumin adsorption onto octacalcium phosphate crystals prepared using different methods, Dent. Mater. J. 39 (2020) 883–891, doi:10.4012/dmj.2019-250.
[31] T. Handa, T. Anada, Y. Honda, H. Yamazaki, K. Kobayashi, N. Kanda, S. Kamakura, S. Echigo, O. Suzuki, The effect of an octacalcium phosphate coprecipitated gelatin composite on the repair of critical-sized rat calvarial defects, Acta Biomater. 8 (2012) 1190–1200, doi:10.1016/j.actbio.2011.12.002.
[32] S. Chiba, T. Anada, K. Suzuki, K. Saito, Y. Shiwaku, N. Miyatake, K. Baba, H. Imaizumi, M. Hosaka, E. Itoi, O. Suzuki, Effect of resorption rate and osteoconductivity of biodegradable calcium phosphate materials on the acquisition of natural bone strength in the repaired bone, J. Biomed. Mater. Res. Part A 104 (2016) 2833–2842, doi:10.1002/jbm.a.35828.
[33] R. Ishiko-Uzuka, T. Anada, K. Kobayashi, T. Kawai, Y. Tanuma, K. Sasaki, O. Suzuki, Oriented bone regenerative capacity of octacalcium phosphate/gelatin composites obtained through two-step crystal preparation method, J. Biomed. Mater. Res. Part B 105 (2017) 1029–1039, doi:10.1002/jbm.b.33640.
[34] S. Sakai, T. Anada, K. Tsuchiya, H. Yamazaki, H.C. Margolis, O. Suzuki, Comparative study on the resorbability and dissolution behavior of octacalcium phosphate, β-tricalcium phosphate, and hydroxyapatite under physiological conditions, Dent. Mater. J. 35 (2016) 216–224, doi:10.4012/dmj.2015-255.
[35] T. Kokubo, H. Takadama, How useful is SBF in predicting *in vivo* bone bioactivity? Biomaterials 27 (2006) 2907–2915, doi:10.1016/j.biomaterials.2006.01.017.
[36] K. Baba, Y. Shiwaku, R. Hamai, Y. Mori, T. Anada, K. Tsuchiya, I. Oizumi, N. Miyatake, E. Itoi, O. Suzuki, Chemical stability-sensitive osteoconductive performance of octacalcium phosphate bone substitute in an ovariectomized rat tibia defect, ACS Appl. Bio Mater. 3 (2020) 1444–1458, doi:10.1021/acsabm.9b01091.
[37] T. Sato, T. Anada, R. Hamai, Y. Shiwaku, K. Tsuchiya, S. Sakai, K. Baba, K. Sasaki, O. Suzuki, Culture of hybrid spheroids composed of calcium phosphate materials and mesenchymal stem cells on an oxygen-permeable culture device to predict *in vivo* bone forming capability, Acta Biomater. 88 (2019) 477–490, doi:10.1016/j.actbio.2019.03.001.
[38] T. Anada, J. Fukuda, Y. Sai, O. Suzuki, An oxygen-permeable spheroid culture system for the prevention of central hypoxia and necrosis of spheroids, Biomaterials 33 (2012) 8430–8441, doi:10.1016/j.biomaterials.2012.08.040.
[39] M. Wakasa, K. Nakanishi, K. Manago, T. Isobe, Y. Eshita, M. Okamoto, T. Isshiki, Fine structure of tooth enamel in the yellowing human teeth: SEM and HRTEM studies, Microsc. Res. Tech. 79 (2016) 14–22, doi:10.1002/jemt.22600.
[40] Q. Wang, S. Ri, H. Tsuda, M. Kodera, K. Suguro, N. Miyashita, Visualization and automatic detection of defect distribution in GaN atomic structure from sampling Moiré phase, Nanotechnology 28 (2017) 455704, doi:10.1088/1361-6528/aa8d83.
[41] D. Hull, D.J. Bacon, Introduction to Dislocations, 5th ed., Butterworth-Heinemann, Oxford, 2011.
[42] A.E. Porter, S.M. Best, W. Bonfield, Ultrastructural comparison of hydroxyapatite and silicon-substituted hydroxyapatite for biomedical applications, J. Biomed. Mater. Res. Part A 68A (2004) 133–141, doi:10.1002/jbm.a.20064.
[43] K. Okuyama, K. Miyama, K. Mizuno, H.P. Bächinger, Crystal structure of (Gly-Pro-Hyp) 9: implications for the collagen molecular model, Biopolymers 97 (2012) 607–616, doi:10.1002/bip.22048.
[44] L. Wang, G.H. Nancollas, Calcium orthophosphates: crystallization and dissolution, Chem. Rev. 108 (2008) 4628–4669, doi:10.1021/cr0782574.
[45] W.E. Brown, M. Mathew, M.S. Tung, Crystal-chemistry of octacalcium phosphate, Prog. Cryst. Growth Charact. 4 (1981) 59–87, doi:10.1016/0146-3535(81)90048-4.
[46] N. Eidelman, L.C. Chow, W.E. Brown, Calcium phosphate saturation levels in ultrafiltered serum, Calcif. Tissue Int. 40 (1987) 71–78, doi:10.1007/BF02555708.
[47] D.G.A. Nelson, J.D. McLean, High-resolution electron microscopy of octacalcium phosphate and its hydrolysis products, Calcif. Tissue Int. 36 (1984) 219–232, doi:10.1007/BF02405321.
[48] M. Iijima, H. Kamemizu, N. Wakamatsu, T. Goto, Y. Doi, Y. Moriwaki, Transition of octacalcium phosphate to hydroxyapatite in solution at pH 7.4 and 37°C, J. Cryst. Growth 181 (1997) 70–78, doi:10.1016/S0022-0248(97)00230-3.
[49] N. Ito, M. Kamitakahara, M. Yoshimura, K. Ioku, Importance of nucleation in transformation of octacalcium phosphate to hydroxyapatite, Mater. Sci. Eng. C 40 (2014) 121–126, doi:10.1016/j.msec.2014.03.034.
[50] R. Tang, W. Wu, M. Haas, G.H. Nancollas, Kinetics of dissolution of β-tricalcium phosphate, Langmuir 17 (2001) 3480–3485, doi:10.1021/la001730n.
[51] M. Ohara, R.C. Reid, Modeling Crystal Growth Rates from Solution, Prentice-Hall, Englewood Cliffs, 1973.
[52] H.H. Teng, Controls by saturation state on etch pit formation during calcite dissolution, Geochim. Cosmochim. Acta 68 (2004) 253–262, doi:10.1016/S0016-7037(03)00423-X.
[53] A.E. Blum, R.A. Yund, A.C. Lasaga, The effect of dislocation density on the dissolution rate of quartz, Geochim. Cosmochim. Acta 54 (1990) 283–297, doi:10.1016/0016-7037(90)90318-F.
[54] K.A. Gross, S. Saber-Samandari, K.S. Heemann, Evaluation of commercial implants with nanoindentation defines future development needs for hydroxyapatite coatings, J. Biomed. Mater. Res. Part B 93 (2010) 1–8, doi:10.1002/jbm.b.31537.
[55] S. Saber-Samandari, K.A. Gross, Amorphous calcium phosphate offers improved crack resistance: a design feature from nature? Acta Biomater. 7 (2011) 4235–4241, doi:10.1016/j.actbio.2011.06.048.
[56] S.S. Bhat, U.V. Waghmare, U. Ramamurty, First-principles study of structure, vibrational, and elastic properties of stoichiometric and calcium-deficient hydroxyapatite, Cryst. Growth Des. 14 (2014) 3131–3141, doi:10.1021/cg5004269.
[57] K. Kobayashi, T. Anada, T. Handa, N. Kanda, M. Yoshinari, T. Takahashi, O. Suzuki, Osteoconductive property of a mechanical mixture of octacalcium phosphate and amorphous calcium phosphate, ACS Appl. Mater. Interfaces 6 (2014) 22602–22611, doi:10.1021/am5067139.
[58] T. Kurobane, Y. Shiwaku, T. Anada, R. Hamai, K. Tsuchiya, K. Baba, M. Iikubo, T. Takahashi, O. Suzuki, Angiogenesis involvement by octacalcium phosphate-gelatin composite-driven bone regeneration in rat calvaria critical-sized defect, Acta Biomater. 88 (2019) 514–526, doi:10.1016/j.actbio.2019.02.021.
[59] T. Nakano, K. Kaibara, Y. Tabata, N. Nagata, S. Enomoto, E. Marukawa, Y. Umakoshi, Unique alignment and texture of biological apatite crystallites in typical calcified tissues analyzed by microbeam X-ray diffractometer system, Bone 31 (2002) 479–487, doi:10.1016/S8756-3282(02)00850-5.
[60] T. Ishimoto, T. Nakano, Y. Umakoshi, M. Yamamoto, Y. Tabata, Degree of biological apatite c-axis orientation rather than bone mineral density controls mechanical function in bone regenerated using recombinant bone morphogenetic protein-2, J. Bone Miner. Res. 28 (2013) 1170–1179, doi:10.1002/jbmr.1825.
[61] O. Suzuki, H. Yagishita, M. Yamazaki, T. Aoba, Adsorption of bovine serum albumin onto octacalcium phosphate and its hydrolyzates, Cells Mater. 5 (1995) 45–54 https://digitalcommons.usu.edu/cellsandmaterials/vol5/iss1/4.
[62] K. Onuma, A. Ito, Cluster growth model for hydroxyapatite, Chem. Mater. 10 (1998) 3346–3351, doi:10.1021/cm980062c.
[63] M. Iijima, J. Moradian-Oldak, Control of octacalcium phosphate and apatite crystal growth by amelogenin matrices, J. Mater. Chem. 14 (2004) 2189–2199, doi:10.1039/B401961J.
[64] E. Davies, K.H. Müller, W.C. Wong, C.J. Pickard, D.G. Reid, J.N. Skepper, M.J. Duer, Citrate bridges between mineral platelets in bone, Proc. Natl. Acad. Sci. U S A. 111 (2014) E1354–E1363, doi:10.1073/pnas.1315080111.
[65] Y. Wang, S. Von Euw, F.M. Fernandes, S. Cassaignon, M. Selmane, G. Laurent, G. Pehau-Arnaudet, C. Coelho, L. Bonhomme-Coury, M.M. Giraud-Guille, F. Babonneau, T. Azais, N. Nassif, Water-mediated structuring of bone apatite, Nat. Mater. 12 (2013) 1144–1153, doi:10.1038/nmat3787.
[66] A. Lotsari, A.K. Rajasekharan, M. Halvarsson, M. Andersson, Transformation of amorphous calcium phosphate to bone-like apatite, Nat. Commun. 9 (2018) 4170, doi:10.1038/s41467-018-06570-x.
[67] S. Von Euw, Y. Wang, G. Laurent, C. Drouet, F. Babonneau, N. Nassif, T. Azais, Bone mineral: new insights into its chemical composition, Sci. Rep. 9 (2019) 8456, doi:10.1038/s41598-019-44620-6.
[68] A. Dey, P.H. Bomans, F.A. Müller, J. Will, P.M. Frederik, G. de With, N.A.J.M. Sommerdijk, The role of prenucleation clusters in surface-induced calcium phosphate crystallization, Nat. Mater. 9 (2010) 1010–1014, doi:10.1038/nmat2900.
[69] H. Zhu, D. Guo, L. Sun, H. Li, D.A.H. Hanaor, F. Schmidt, K. Xu, Nanostructural insights into the dissolution behavior of Sr-doped hydroxyapatite, J. Eur. Ceram. Soc. 38 (2018) 5554–5562, doi:10.1016/j.jeurceramsoc.2018.07.056.
[70] A.J. Nathanael, S.I. Hong, D. Mangalaraj, N. Ponpandian, P.C. Chen, Template-free growth of novel hydroxyapatite nanorings: formation mechanism and their enhanced functional properties, Cryst. Growth Des. 12 (2012) 3565–3574, doi:10.1021/cg3003959.
[71] I.S. Yahia, M. Shkir, S. AlFaify, V. Ganesh, H.Y. Zahran, M. Kilany, Facile microwave-assisted synthesis of Te-doped hydroxyapatite nanorods and nanosheets and their characterizations for bone cement applications, Mater. Sci. Eng. C 72 (2017) 472–480, doi:10.1016/j.msec.2016.11.074.